

# Machine Learning for MU-MIMO Receive Processing in OFDM Systems

Mathieu Goutay, *Student Member, IEEE*, Fayçal Ait Aoudia, *Member, IEEE*, Jakob Hoydis, *Senior Member, IEEE*, and Jean-Marie Gorce, *Senior Member, IEEE*

**Abstract**—Machine learning (ML) starts to be widely used to enhance the performance of multi-user multiple-input multiple-output (MU-MIMO) receivers. However, it is still unclear if such methods are truly competitive with respect to conventional methods in realistic scenarios and under practical constraints. In addition to enabling accurate signal reconstruction on realistic channel models, MU-MIMO receive algorithms must allow for easy adaptation to a varying number of users without the need for retraining. In contrast to existing work, we propose an ML-enhanced MU-MIMO receiver that builds on top of a conventional linear minimum mean squared error (LMMSE) architecture. It preserves the interpretability and scalability of the LMMSE receiver, while improving its accuracy in two ways. First, convolutional neural networks (CNNs) are used to compute an approximation of the second-order statistics of the channel estimation error which are required for accurate equalization. Second, a CNN-based demapper jointly processes a large number of orthogonal frequency-division multiplexing (OFDM) symbols and subcarriers, which allows it to compute better log likelihood ratios (LLRs) by compensating for channel aging. The resulting architecture can be used in the up- and downlink and is trained in an end-to-end manner, removing the need for hard-to-get perfect channel state information (CSI) during the training phase. Simulation results demonstrate consistent performance improvements over the baseline which are especially pronounced in high mobility scenarios.

**Index Terms**—Multi-user MIMO detection, OFDM, channel estimation, deep learning, neural networks

## I. INTRODUCTION

Machine learning (ML) has transformed many research areas in the past decade but only started to revolutionize wireless communications in recent years with applications to end-to-end learning [1], channel coding [2], resource management [3], and many others [4]. In particular, the application of ML to the physical layer has led to promising results on realistic channels [5] and this technology is now perceived as a major enabler of future generations of wireless networks [6]. Another key technique is the use of multi-user multiple-input multiple-output (MU-MIMO) systems, where spatial multiplexing is leveraged to increase both the channel capacity and the number of users that can be served simultaneously [7]. One of the main challenges related to the deployment of such systems is the complexity of the receive processing, which grows with the number of antennas and users. Traditional non-linear MIMO

detection methods offer strong performance but quickly become impractical in large systems. For example, maximum a posteriori detection is optimal but known to be NP-hard, and sphere decoders have exponential worst-case complexity [8]. The conventional solution to tackle this problem uses linear detectors that are computationally tractable, but suffers from performance degradation on ill-conditioned channels. Therefore, the development of new receivers that combine low complexity and high performance is crucial to unlock the full potential of MU-MIMO.

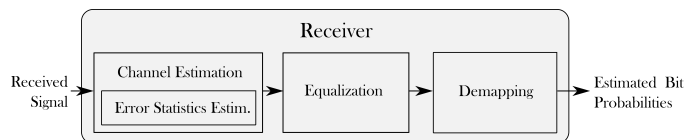


Fig. 1: Traditional receiver architecture.

An attractive research direction is to apply ML techniques to improve MIMO reception. Essentially, two distinct approaches are emerging. The first one is to consider a single processing block in the typical receiver architecture depicted in Fig. 1 and to augment it with ML. The second approach is to replace multiple blocks with a single ML component, such as a neural network (NN). The former has the advantages of remaining interpretable and scalable to any number of users [9], but is not trained to optimize the end-to-end receiver performance and requires ground truth measurements that are not available in practice. The latter has shown promising results [10], but is very computationally expensive and acts as a black-box that cannot be adapted to changing number of users or transmit antennas without full retraining.

In this paper, we introduce a new hybrid strategy, where multiple ML components are jointly trained to enhance a conventional MU-MIMO receiver architecture. The goal is to combine the interpretability of the first approach, the efficiency of the second one, and the flexibility of traditional receivers. The resulting architecture is easily scalable to any number of users and is composed of components that are individually interpretable and of reasonable complexity. We are interested in both uplink and downlink orthogonal frequency-division multiplexing (OFDM) transmissions. Our solution additionally exploits the OFDM structure to counteract two known drawbacks of conventional receivers that are overlooked in the current literature. First, it improves the prediction of the channel estimation error statistics, that can only be obtained for the pilot signals in a standard receiver, resulting in largely

F. Ait Aoudia and J. Hoydis are with Nokia Bell Labs, Paris-Saclay, 91620 Nozay, France (e-mail: {faycal.ait\_aoudia, jakob.hoydis}@nokia-bell-labs.com).

J.-M. Gorce is with Univ. Lyon, INSA Lyon, Inria, CITI, 69100 Villeurbanne, France (e-mail: jean-marie.gorce@insa-lyon.fr).

M. Goutay is with both institutions (e-mail: mathieu.goutay@nokia.com).

sub-optimal detection accuracy. Motivated by the recent successes of convolutional neural networks (CNNs) in physical layer tasks [11], [12], we use CNNs to predict those channel estimation error statistics for every position of the OFDM time-frequency grid. In contrast to the traditional approach that is based on mathematical models, the CNNs learn the error statistics from the data during training. The second improvement is the demapper, which computes log likelihood ratios (LLRs) over the transmitted bits. We propose a CNN-based demapper that operates on the entire OFDM grid, unlike a traditional demapper that operates on individual resource elements (REs). In doing so, our demapper is able to better cope with the residual distortions of the equalized signal. The resulting ML-enhanced receiver is optimized such that all ML components are jointly trained to maximize the information rate of the transmission [13].

The proposed architecture is evaluated on 3rd Generation Partnership Project (3GPP)-compliant channel models with two different pilot configurations supported by the 5G new radio (NR) specifications. Both uplink and downlink transmissions are studied using time-division duplexing (TDD). We compare the coded bit error rate (BER) achieved by different schemes for user speeds ranging from 0 to 130 km h<sup>-1</sup>. Two baselines were implemented, the first one being a traditional receiver implementing a linear minimum mean squared error (LMMSE) channel estimation and an LMMSE equalizer. The second baseline also uses LMMSE equalization, but is provided with perfect channel knowledge at pilot positions and the exact second order statistics of the channel estimation errors. Our results show that the gains provided by the ML-enhanced receiver increase with the user speed, with small BER improvements at low speeds and significant ones at high speeds. We have also observed that the gains in the uplink are more pronounced than in the downlink, due to channel aging which significantly penalizes the downlink precoding scheme.

### Related literature

Most of the published literature focuses exclusively on the equalization step, which estimates the sent signals from the received ones. Although performance gains over traditional equalizers were shown, the solutions typically assume perfect channel state information (CSI), are too computationally demanding to be practical, or are trained and evaluated over too simplistic channel models [9], [14–17]. For example, the OAMP-Net equalizer proposed in [15] performs ten matrix inversions to equalize one signal and the MMNet architecture presented in [16] needs to be trained for every channel realization. Moreover, these papers assume perfect CSI, which is not available in practice. For this reason, there is another line of research targeting improved channel estimation [11], [18], [19]. However, they require ground-truth of the channel realizations during training, which can only be approximated with costly measurement campaigns in practice. Finally, it has also been proposed to improve the estimation of the bit probabilities by replacing the demapper with a NN, but this solution has only been studied for single-input single-output (SISO) setups [20–23]. In this work, we propose a

complete MU-MIMO receiver that both improves the channel estimation error statistics and the predicted LLRs without requiring perfect CSI knowledge at training.

More recent papers also leverage a single NN to jointly perform multiple processing steps. This idea has first been proposed in [24] to perform joint channel estimation and equalization in a SISO setup. This work has then been extended by additionally learning the demapper and operating directly on time-domain samples [10], [25]. The DeepRX architecture presented in [12] shows impressive results on single-input multiple-output (SIMO) channels while being 5G compliant. Another standard-compliant receiver has been proposed for Wi-Fi communications using both synthetic and real-world data [26]. Regarding MIMO transmissions, a special form of recurrent neural network called reservoir computing has been leveraged in [27] to process time-domain OFDM signals. The DeepRX receiver has also been extended with a so-called transformation layer to handle MIMO transmissions [10]. Their CNN-based solution is fed with frequency-domain signals and outputs LLRs for the transmitted bits. DeepRX MIMO shows important gains on single-user (SU)-MIMO channels, but remains very computationally expensive. Compared to our solution, the main disadvantages of these NN-based MIMO receivers are their lack of scalability and interpretability. They are tailored for a specific number of users or transmit antennas, and the CSI needed for downlink precoding can not be easily extracted.

The rest of this paper is structured as follows : In Section II, we introduce the channel model and both the uplink and downlink baseline receiver architectures. In Section III, we highlight two limitations of these architectures and detail how we address them using CNNs. Section IV provides simulation results to compare the various schemes. Section V concludes the paper.

**Notations :**  $\mathbb{R}$  and  $\mathbb{C}$  denotes the set of real and complex numbers. Tensors/matrices are denoted by bold upper-case letters and vectors are denoted by bold lower-case letters. We denote by  $\mathbf{T}_{a,b} \in \mathbb{C}^{N_c \times N_d}$  ( $t_{a,b,c} \in \mathbb{C}^{N_d}$ ,  $t_{a,b,c,d} \in \mathbb{C}$ ) the matrix (vector, scalar) formed by slicing the tensor  $\mathbf{T} \in \mathbb{C}^{N_a \times N_b \times N_c \times N_d}$  along the first two (three, four) dimensions. The notation  $\mathbf{T}^{(k)}$  indicates that the quantity at hand is only considered for the  $k^{\text{th}}$  user, and  $\mathbf{v}_{-a}$  corresponds to the vector  $\mathbf{v}$  from which the  $a^{\text{th}}$  element was removed.  $\|\mathbf{M}\|_{\text{F}}$  denotes the Frobenius norm of  $\mathbf{M}$ .  $\text{Card}(\mathcal{S})$  denotes the number of elements in a set  $\mathcal{S}$ ,  $\text{vec}(\cdot)$  the vectorization operator, and  $\odot$  the element-wise product.  $(\cdot)^{\text{T}}$ ,  $(\cdot)^{\text{H}}$ , and  $(\cdot)^*$  denote respectively the transpose, conjugate transpose, and element-wise conjugate operator.  $\mathbf{I}_N$  is the  $N \times N$  identity matrix and  $\mathbb{1}_{N \times M}$  is the  $N \times M$  matrix where all elements are set to 1. The imaginary unit is  $j$ , such that  $j^2 = -1$ .

## II. SYSTEM MODEL

We consider a multi-user multiple-input multiple-output (MU-MIMO) system, where  $N_k$  single-antenna users communicate with a base station (BS) equipped with  $N_m$  antennas in the uplink and downlink. The number of bits transmitted per channel use is denoted by  $B$  and  $\mathcal{C} = \{c_1, \dots, c_{2^B}\} \in \mathbb{C}^{2^B}$

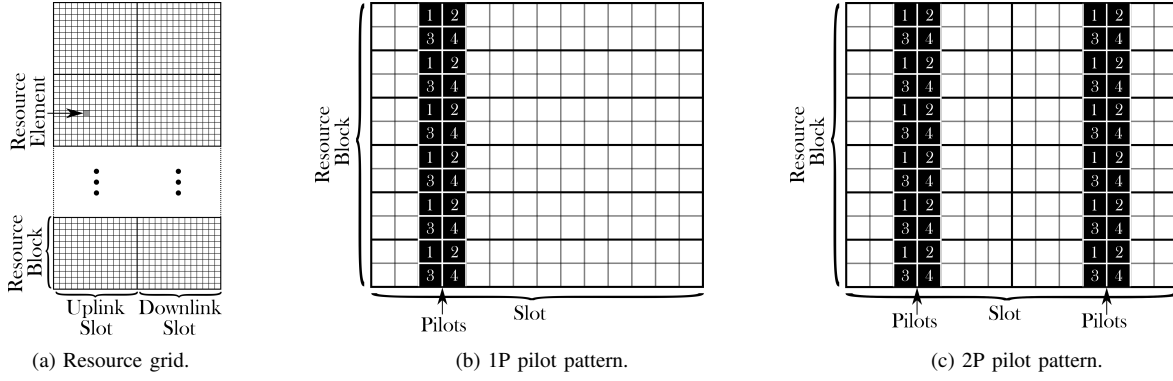


Fig. 2: Pilots are arranged on the resource grid (RG) according to two different patterns, where each number corresponds to a different transmitter.

is the quadrature amplitude modulation (QAM) constellation used to transmit data. This section introduces the channel model and the baselines against which the proposed approach is benchmarked.

#### A. Channel model

An OFDM waveform is considered with  $N_f$  subcarriers, divided into resource blocks consisting of twelve adjacent subcarriers. Adjacent OFDM symbols are gathered into groups of size  $N_t$ , referred to as *slots*. The entire frequency-time grid is called the RG and contains all REs, as shown in Fig. 2a. The channel coefficients form a 4-dimensional tensor denoted by  $\mathbf{H} \in \mathbb{C}^{N_f \times 2N_t \times N_m \times N_k}$ , such that  $\mathbf{H}_{f,t} \in \mathbb{C}^{N_m \times N_k}$  is the channel matrix at RE  $(f, t)$ , and  $\mathbf{h}_{f,t,k} \in \mathbb{C}^{N_m}$  is the channel vector at RE  $(f, t)$  and for user  $k$ . Duplexing is achieved through TDD, such that a slot is either assigned to the uplink or downlink in an alternating fashion, as illustrated in Fig. 2a. More precisely, the first slot is assigned to the uplink and the second slot is assigned to the downlink. It is assumed that channel reciprocity holds, i.e.,  $\mathbf{H}_{f,t}$  refers as well to the uplink or the downlink channel. To enable channel estimation, a transmitter sends pilot signals on dedicated REs according to a predefined pilot pattern. We assume, without loss of generality, that all pilots are equal to one. Two pilot patterns are considered in this work, referred to as the 1P and 2P pilot patterns, which respectively contain pilots on two or four symbols within a slot. Fig. 2b and 2c respectively show the 1P and 2P pilot patterns over a resource block assuming 4 users. The set of REs carrying pilots for a user  $k \in \{1, \dots, N_k\}$  is denoted by  $\mathcal{P}^{(k)}$  and the numbers of subcarriers and symbols carrying pilots are respectively denoted by  $N_{P_f}$  and  $N_{P_t}$ . As an example, if the 1P pattern shown in Fig. 2b is used with  $N_f = 12$ , the positions (subcarrier, symbol) of all REs carrying pilots for user 1 are denoted by  $\mathcal{P}^{(1)} = \{(1, 3), (3, 3), (5, 3), (7, 3), (9, 3), (11, 3)\}$ , resulting in  $N_{P_f} = 6$  and  $N_{P_t} = 1$ . Note that when a RE is allocated to a user for the transmission of a pilot, other users do not transmit any signal (data nor pilot) on that RE. As a consequence, pilots do not experience any interference. The noise power is denoted by  $\sigma^2$  and assumed equal for all users and all REs. In the following, perfect power

control is assumed over the RG such that the mean energy corresponding to a single BS antenna and a single user is one, i.e.,  $\mathbb{E}[|h_{f,t,m,k}|^2] = 1$ . The signal-to-noise ratio (SNR) of the transmission is defined as

$$\text{SNR} = 10 \log \left( \frac{\mathbb{E}[|h_{f,t,m,k}|^2]}{\sigma^2} \right) = 10 \log \left( \frac{1}{\sigma^2} \right) \text{ [dB]}. \quad (1)$$

#### B. Uplink baseline

In uplink, the BS aims to recover the bits transmitted simultaneously by the  $N_k$  users on RE carrying data. The tensors of transmitted and received signals of all users are respectively denoted by  $\mathbf{X} \in \mathbb{C}^{N_f \times 2N_t \times N_k}$  and  $\mathbf{Y} \in \mathbb{C}^{N_f \times 2N_t \times N_m}$ . In this scenario, only the uplink slot is used and therefore all signals with indices  $t > N_t$  are ignored and the corresponding values are set to 0. The transfer function of the uplink channel for a RE  $(f, t)$  is

$$\mathbf{y}_{f,t} = \mathbf{H}_{f,t} \mathbf{x}_{f,t} + \mathbf{n}_{f,t} \quad (2)$$

where  $\mathbf{n}_{f,t} \sim \mathcal{CN}(\mathbf{0}, \sigma^2 \mathbf{I}_{N_m})$  is the noise vector. The architecture of the uplink system is shown in Fig. 3, where the IFFT (FFT) operation and the addition (removal) of the cyclic prefix before (after) the channel are not shown for clarity. The channel estimation, equalization, and demapping stages of the baseline will be explained in the following sections.

1) *Channel estimation*: As the pilots are assumed to be orthogonal, LMMSE channel estimation can be carried out for each user independently. The channel covariance matrix providing the spatial, temporal, and spectral correlations between all REs carrying pilots is denoted by  $\Sigma \in \mathbb{C}^{N_{P_f} N_{P_t} N_m \times N_{P_f} N_{P_t} N_m}$ . In the following, it is assumed that the precise local statistics of the receivers are not available. The channel and receiver statistics are therefore averaged over the entire cell, resulting in a zero-mean channel, and a discussion on how these statistics can be obtained is provided in Section II-D. For a user  $k \in \{1, \dots, N_k\}$ , the LMMSE channel estimate at REs carrying pilots is denoted by  $\widehat{\mathbf{H}}_{\mathcal{P}^{(k)}}^{(k)} \in \mathbb{C}^{N_{P_f} \times N_{P_t} \times N_m}$  and given by

$$\text{vec} \left( \widehat{\mathbf{H}}_{\mathcal{P}^{(k)}}^{(k)} \right) = \Sigma \left( \Sigma + \sigma^2 \mathbf{I}_{N_{P_f} N_{P_t} N_m} \right)^{-1} \text{vec} \left( \mathbf{Y}_{\mathcal{P}^{(k)}}^{(k)} \right) \quad (3)$$

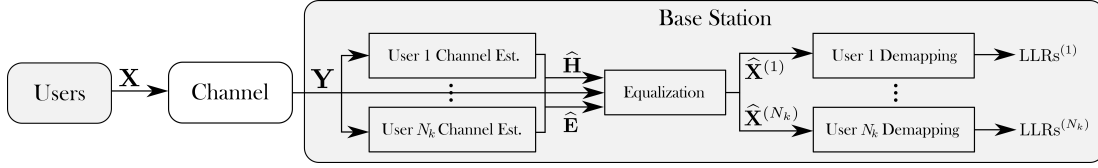


Fig. 3: Architecture of the uplink communication system.

where  $\mathbf{Y}_{\mathcal{P}^{(k)}}^{(k)} \in \mathbb{C}^{N_{P_f} \times N_{P_t} \times N_m}$  is the tensor of received pilots for user  $k$ . Channel estimation could also be performed at REs carrying data [21], but this would require knowledge of the channel statistics at those REs, which are typically not available in practice.

Inspired by the 3GPP guidelines [28], the channel estimates for all REs are computed by first linearly interpolating the estimates from REs carrying pilots in the frequency dimension and then using the estimate at the nearest interpolated resource element (NIRE) on the neighboring REs. It is also possible to leverage temporal linear interpolation between the OFDM symbols carrying pilots when the 2P pilot pattern is used. The so-obtained tensor of channel estimates is denoted by  $\hat{\mathbf{H}}^{(k)} \in \mathbb{C}^{N_f \times 2N_t \times N_m}$ . The overall channel estimation for all users  $\hat{\mathbf{H}} \in \mathbb{C}^{N_f \times 2N_t \times N_m \times N_k}$  is obtained by stacking the channel estimates of all users. Since only the uplink slot is considered here, the channel estimates for the last  $N_t$  symbols (downlink slot) are set to be null. The channel estimation error is denoted by  $\tilde{\mathbf{H}}$  and is such that  $\mathbf{H} = \hat{\mathbf{H}} + \tilde{\mathbf{H}}$ . For a RE  $(f, t)$ , we define

$$\mathbf{E}_{f,t} := \mathbb{E} \left[ \tilde{\mathbf{H}}_{f,t} \tilde{\mathbf{H}}_{f,t}^H \right] \quad (4)$$

as the sum of the *spatial* channel estimation error covariance matrices from all users.

2) *Equalization*: The widely used LMMSE equalizer is leveraged, as it maximizes the post-equalization SNR among all linear operators. However, as computing a dedicated LMMSE operator for each RE is infeasible in practice due to prohibitive complexity, we resort to a grouped-LMMSE equalizer, i.e., a single LMMSE operator is applied to a group of adjacent REs spanning multiple subcarriers  $f \in \{F_b, \dots, F_e\}$  and symbols  $t \in \{T_b, \dots, T_e\}$ . Under this assumption, the LMMSE operator for the group of REs spanning  $\{F_b, \dots, F_e\} \times \{T_b, \dots, T_e\}$  is

$$\mathbf{W}_{f,t} = \left( \sum_{f'=F_b}^{F_e} \sum_{t'=T_b}^{T_e} \hat{\mathbf{H}}_{f',t'}^H \right) \left( \sum_{f'=F_b}^{F_e} \sum_{t'=T_b}^{T_e} \hat{\mathbf{H}}_{f',t'} \hat{\mathbf{H}}_{f',t'}^H + \mathbf{E}_{f',t'} + \sigma^2 \mathbf{I}_{N_m} \right)^{-1} \quad (5)$$

where  $\mathbf{W}_{f,t} \in \mathbb{C}^{N_k \times N_m}$  is constant over  $\{F_b, \dots, F_e\} \times \{T_b, \dots, T_e\}$  (as derived in Appendix A).

The post-equalization channel is expected to be an additive noise channel. More precisely, for any RE  $(f, t)$ , the demapper expects the output of the equalizer  $\hat{\mathbf{x}}_{f,t} \in \mathbb{C}^{N_k}$  to be such that  $\hat{\mathbf{x}}_{f,t} = \mathbf{x}_{f,t} + \mathbf{z}_{f,t}$  where  $\mathbf{z}_{f,t}$  is an additive noise term. However, this decomposition is not achieved by the LMMSE equalizer (see Section 1.6.1 of [29] for a more detailed discussion). To obtain such a post-equalized channel, the following diagonal matrix is applied to the output of the LMMSE equalizer

$$\mathbf{D}_{f,t} = \left( \left( \mathbf{W}_{f,t} \hat{\mathbf{H}}_{f,t} \right) \odot \mathbf{I}_{N_k} \right)^{-1} \quad (6)$$

which re-scales the equalizer output so that the post-equalization SNR remains maximized. For a RE  $(f, t) \in \{F_b, \dots, F_e\} \times \{T_b, \dots, T_e\}$ , the equalized vector  $\hat{\mathbf{x}}_{f,t} \in \mathbb{C}^{N_k}$  is computed by

$$\hat{\mathbf{x}}_{f,t} = \mathbf{D}_{f,t} \mathbf{W}_{f,t} \mathbf{y}_{f,t}. \quad (7)$$

The equalized symbols of user  $k$  are denoted by  $\hat{\mathbf{X}}^{(k)} \in \mathbb{C}^{N_f \times N_t}$ , as shown in Fig. 3.

3) *Demapping*: For a RE  $(f, t)$ , let us denote by  $\mathbf{w}_{f,t,k}$  the column vector made of the  $k^{\text{th}}$  line of the matrix  $\mathbf{W}_{f,t}$  and by  $\mathbf{H}_{f,t,-k}$  the tensor made of the channel coefficients of all users except user  $k$ . After equalization, the uplink channel can be viewed as  $N_f N_t N_k$  parallel additive noise channels that can be demodulated independently for every RE and every user. For a RE  $(f, t)$  and user  $k$ , the post-equalization channel is expressed as

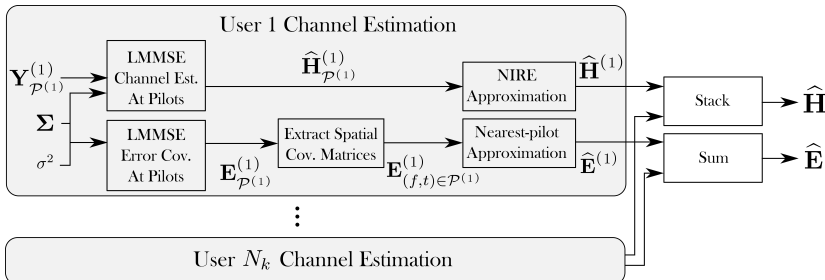


Fig. 4: Uplink channel estimation.

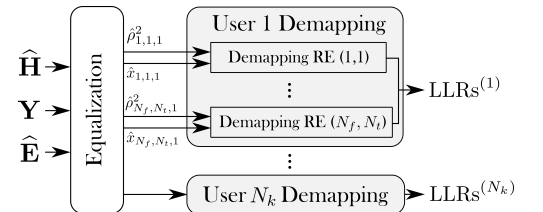


Fig. 5: Uplink demapping

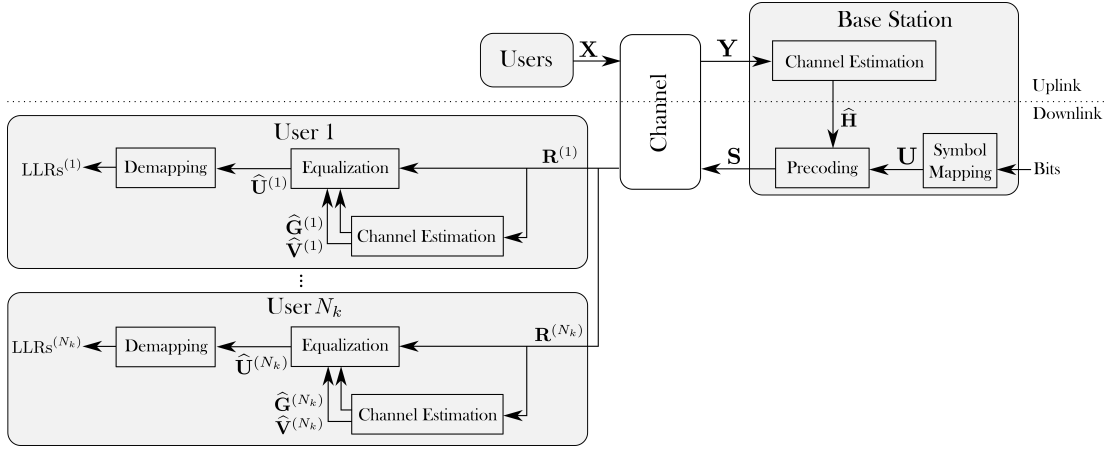


Fig. 6: Architecture of the downlink communication system.

$$\hat{x}_{f,t,k} = x_{f,t,k} + \underbrace{\frac{\mathbf{w}_{f,t,k}^T \left( \hat{\mathbf{H}}_{f,t,-k} \mathbf{x}_{f,t,-k} + \tilde{\mathbf{H}}_{f,t} \mathbf{x}_{f,t} + \mathbf{n}_{f,t} \right)}{\mathbf{w}_{f,t,k}^T \hat{\mathbf{h}}_{f,t,k}}}_{z_{f,t,k}} \quad (8)$$

where the noise  $z_{f,t,k}$  includes both the interference and the noise experienced by user  $k$ . Its variance is given by

$$\begin{aligned} \rho_{f,t,k}^2 &= \mathbb{E} [z_{f,t,k}^* z_{f,t,k}] \\ &= \frac{\mathbf{w}_{f,t,k}^H \left( \hat{\mathbf{H}}_{f,t,-k} \hat{\mathbf{H}}_{f,t,-k}^H + \mathbf{E}_{f,t} + \sigma^2 \mathbf{I}_{N_m} \right) \mathbf{w}_{f,t,k}}{\mathbf{w}_{f,t,k}^H \hat{\mathbf{h}}_{f,t,k} \hat{\mathbf{h}}_{f,t,k}^H \mathbf{w}_{f,t,k}}. \end{aligned} \quad (9)$$

We denote by  $\mathcal{C}_{b,0}$  ( $\mathcal{C}_{b,1}$ ) the subset of  $\mathcal{C}$  which contains all symbols with the  $b^{\text{th}}$  bit set to 0 (1). Assuming the noise  $z_{f,t,k}$  is Gaussian<sup>1</sup>, the LLRs of the  $b^{\text{th}}$  bit transmitted by user  $k$  on the RE  $(f, t)$  is given by

$$\text{LLR}_{f,t,k}^{\text{UL}}(b) = \ln \left( \frac{\sum_{c \in \mathcal{C}_{b,1}} \exp \left( -\frac{1}{\rho_{f,t,k}^2} |\hat{x}_{f,t,k} - c|^2 \right)}{\sum_{c \in \mathcal{C}_{b,0}} \exp \left( -\frac{1}{\rho_{f,t,k}^2} |\hat{x}_{f,t,k} - c|^2 \right)} \right). \quad (10)$$

The equalization and demapping process is schematically shown in Fig. 5.

### C. Downlink baseline

The BS aims to simultaneously transmit to  $N_k$  users on all REs of the downlink slot. The signal transmitted by the BS is precoded to mitigate interference. We remind that downlink transmissions occur after the uplink slot, as shown in Fig. 2a. Let us denote by  $\mathbf{U} \in \mathbb{C}^{N_f \times 2N_t \times N_k}$  and by  $\mathbf{S} \in \mathbb{C}^{N_f \times 2N_t \times N_m}$  the tensors of unprecoded and precoded symbols, respectively. We denote by  $\mathbf{R} \in \mathbb{C}^{N_f \times 2N_t \times N_k}$  the tensor of symbols received by the  $N_k$  users. Those quantities are only relevant on the downlink slot and therefore are considered null on the first  $N_t$  symbols, i.e.,  $\mathbf{u}_{f,t} = \mathbf{s}_{f,t} = \mathbf{r}_{f,t} = \mathbf{0} \quad \forall (f, t) \in \{1, \dots, N_f\} \times \{1, \dots, N_t\}$ . The downlink transfer function of the channel for a RE  $(f, t)$  is

$$\mathbf{r}_{f,t} = \mathbf{H}_{f,t}^H \mathbf{s}_{f,t} + \mathbf{q}_{f,t} \quad (11)$$

<sup>1</sup>This is not true in general as the interference and channel estimation errors are not Gaussian distributed.

where  $\mathbf{q}_{f,t} \sim \mathcal{CN}(\mathbf{0}, \sigma^2 \mathbf{I}_{N_k})$  is the noise vector, considered null in the first  $N_t$  symbols. For convenience, the noise variance  $\sigma^2$  is assumed to be the same as in the uplink. Fig. 6 shows the architecture of the downlink system, where the IFFT (FFT) operation and the addition (removal) of the cyclic prefix before (after) the channel are again not shown for clarity. In the rest of this section, we detail the precoding, channel estimation and equalization, and demapping steps.

1) *Precoding*: Precoding requires estimation of the downlink channel. As TDD is used, we can exploit channel reciprocity so that the downlink channel can be estimated using the nearest-pilot approach, i.e.,  $\hat{\mathbf{H}}_{f, N_t+1 \leq t \leq 2N_t} = \hat{\mathbf{H}}_{f, N_t}$ . Precoding is achieved by exploiting the uplink-downlink duality [30], which results in using  $\mathbf{W}_{f,t}^H$  as precoding matrix that can be computed using (5). Normalization is performed to ensure that the average energy per transmitted symbol equals one, by applying the diagonal matrix

$$\mathbf{N}_{f,t} = \left( (\mathbf{W}_{f,t} \mathbf{W}_{f,t}^H) \odot \mathbf{I}_{N_k} \right)^{-\frac{1}{2}} \quad (12)$$

leading to the precoded signal

$$\mathbf{s}_{f,t} = \mathbf{N}_{f,t} \mathbf{W}_{f,t}^H \mathbf{u}_{f,t}. \quad (13)$$

The channel transfer function (11) can be rewritten as

$$\mathbf{r}_{f,t} = \underbrace{\mathbf{H}_{f,t}^H \mathbf{N}_{f,t} \mathbf{W}_{f,t}^H}_{\mathbf{G}_{f,t}} \mathbf{u}_{f,t} + \mathbf{q}_{f,t} \quad (14)$$

where  $\mathbf{G}_{f,t} \in \mathbb{C}^{N_k \times N_k}$  is referred to as the *equivalent* downlink channel for the RE  $(f, t)$ . Each user  $k$  receives its signal  $r_{f,t}^{(k)}$  and the corresponding channel, i.e., the  $k^{\text{th}}$  row of  $\mathbf{G}_{f,t}$ , is denoted by  $\mathbf{g}_{f,t}^{(k)\top} \in \mathbb{C}^{N_k}$ . Finally, the equivalent channel experienced by user  $k$  for the entire RG is denoted by  $\mathbf{G}^{(k)} \in \mathbb{C}^{N_f \times 2N_t \times N_k}$ .

2) *Channel estimation and equalization*: To enable estimation of the equivalent downlink channel by the users, pilot signals are transmitted by the BS using the same pilot patterns as in the uplink (Fig. 2). Each user  $k$  estimates its equivalent channel  $\hat{\mathbf{G}}^{(k)} \in \mathbb{C}^{N_f \times 2N_t \times N_k}$ , where for a given RE  $(f, t)$ , the element  $\hat{g}_{f,t,k}^{(k)}$  corresponds to the main channel coefficient, whereas the elements  $\hat{g}_{f,t,i}^{(k)}$ ,  $i \neq k$  correspond to the

interference channel coefficients. As in the uplink, LMMSE estimation, followed by spectral and possibly temporal interpolation, is used, but it is assumed that the elements of  $\hat{\mathbf{g}}_{f,t}^{(k)}$  are uncorrelated. Therefore, channel estimation is performed independently for the main channel and each interference channel, enabling easy scalability to any number of interferers. The covariance matrices used to estimate the main channel and one of the interfering channels of a given user are denoted by  $\mathbf{\Omega} \in \mathbb{C}^{N_{P_f} N_{P_t} \times N_{P_f} N_{P_t}}$  and by  $\mathbf{\Psi} \in \mathbb{C}^{N_{P_f} N_{P_t} \times N_{P_f} N_{P_t}}$ , respectively, and are equal for all users and interfering channels. The tensor of the equivalent channel estimation error for user  $k$  is denoted by  $\tilde{\mathbf{G}}^{(k)} \in \mathbb{C}^{N_f \times 2N_t \times N_k}$ , and is such that  $\mathbf{G}^{(k)} = \tilde{\mathbf{G}}^{(k)} + \hat{\mathbf{G}}^{(k)}$ . The estimation error variances for the main and the  $i^{\text{th}}$  interfering channel of user  $k$  are respectively denoted by  $v_{f,t,k}^{(k)} := \mathbb{E} \left[ |\tilde{g}_{f,t,k}^{(k)}|^2 \right]$  and  $v_{f,t,i}^{(k)} := \mathbb{E} \left[ |\tilde{g}_{f,t,i}^{(k)}|^2 \right]$ . Similarly, we denote by  $\mathbf{V}^{(k)} \in \mathbb{R}^{N_f \times N_t \times N_k}$  the tensor of estimated error variances for user  $k$ , as shown in Fig. 6. An estimation of the transmitted unprecoded symbol for user  $k$  is computed by equalizing the received signal as follows

$$\hat{u}_{f,t}^{(k)} = \frac{r_{f,t}^{(k)}}{\hat{g}_{f,t,k}^{(k)}}. \quad (15)$$

3) *Demapping*: The post-equalization downlink channel can be seen as  $N_f \times N_t \times N_k$  parallel additive noise channels. More precisely, for a user  $k \in \{1, \dots, N_k\}$  and RE  $(f, t)$ ,

$$\hat{u}_{f,t}^{(k)} = u_{f,t,k} + \underbrace{\frac{\tilde{g}_{f,t,k}^{(k)} u_{f,t,k} + \mathbf{g}_{f,t,-k}^{(k) \text{T}} \mathbf{u}_{f,t,-k} + q_{f,t,k}}{\hat{g}_{f,t,k}^{(k)}}}_{o_{f,t,k}} \quad (16)$$

where  $o_{f,t,k}$  comprises the channel noise and interference and has variance

$$\begin{aligned} \tau_{f,t,k}^2 &= \mathbb{E} \left[ o_{f,t,k}^* o_{f,t,k} \right] \\ &= \frac{v_{f,t,k}^{(k)} + \hat{\mathbf{g}}_{f,t,-k}^{(k) \text{H}} \hat{\mathbf{g}}_{f,t,-k}^{(k)} + \sum_{i=1, i \neq k}^{N_k} v_{f,t,i}^{(k)} + \sigma^2}{|\hat{g}_{f,t,k}^{(k)}|^2}. \end{aligned} \quad (17)$$

Assuming  $o_{f,t,k}$  is Gaussian distributed<sup>2</sup>, the LLR for the  $b^{\text{th}}$  bit transmitted to user  $k$  on RE  $(f, t)$  is given by

$$\text{LLR}_{f,t,k}^{\text{DL}}(b) = \ln \left( \frac{\sum_{c \in \mathcal{C}_{b,1}} \exp \left( -\frac{1}{\tau_{f,t,k}^2} |\hat{u}_{f,t,k} - c|^2 \right)}{\sum_{c \in \mathcal{C}_{b,0}} \exp \left( -\frac{1}{\tau_{f,t,k}^2} |\hat{u}_{f,t,k} - c|^2 \right)} \right). \quad (18)$$

#### D. Estimation of the required statistics

The baselines described above require the knowledge of the covariance matrices  $\mathbf{\Sigma}$ ,  $\mathbf{\Omega}$ , and  $\mathbf{\Psi}$  which provide the spatial, time, and spectral correlations between the REs carrying pilots. These matrices can be set based on models or can be empirically estimated by constructing large datasets of uplink, downlink, and interfering pilot signals, as is done in this paper. The channel estimation error covariances  $\mathbf{E}_{f,t}$ , defined in (4), also need to be estimated to compute both the

uplink equalization matrices  $\mathbf{W}_{f,t}$  and the downlink precoding matrices  $\mathbf{W}_{f,t}^{\text{H}}$ . Focusing on REs carrying pilots, the estimation error covariance for a user  $k$  is given by

$$\begin{aligned} \mathbf{E}_{\mathcal{P}^{(k)}}^{(k)} &= \mathbb{E} \left[ \text{vec} \left( \tilde{\mathbf{H}}_{\mathcal{P}^{(k)}}^{(k)} \right) \text{vec} \left( \tilde{\mathbf{H}}_{\mathcal{P}^{(k)}}^{(k)} \right)^{\text{H}} \right] \\ &= \mathbf{\Sigma} - \mathbf{\Sigma} (\mathbf{\Sigma} + \sigma^2)^{-1} \mathbf{\Sigma} \end{aligned} \quad (19)$$

where  $\tilde{\mathbf{H}}_{\mathcal{P}^{(k)}}^{(k)}$  is the channel estimation error at REs carrying pilots. However, we are only interested in the *spatial* channel estimation error correlations, whereas (19) provides the correlations of channel estimation errors between all the receive antennas, subcarriers, and symbols. For a single pilot position  $(f, t) \in \mathcal{P}^{(k)}$ , this spatial correlation matrix is defined by

$$\mathbf{E}_{(f,t) \in \mathcal{P}^{(k)}}^{(k)} = \mathbb{E} \left[ \left( \tilde{\mathbf{h}}_{(f,t) \in \mathcal{P}^{(k)}}^{(k)} \right) \left( \tilde{\mathbf{h}}_{(f,t) \in \mathcal{P}^{(k)}}^{(k)} \right)^{\text{H}} \right] \in \mathbb{C}^{N_m \times N_m} \quad (20)$$

and can be extracted from  $\mathbf{E}_{\mathcal{P}^{(k)}}^{(k)}$ . To estimate  $\mathbf{E}_{f,t}$  for REs carrying data, a nearest-pilot approach is leveraged, which sets the value  $\mathbf{E}_{f,t}$  for a RE carrying a data signal to the one of the nearest RE carrying a pilot signal. The so-obtained estimation is denoted by  $\hat{\mathbf{E}}_{f,t}^{(k)}$  for a RE  $(f, t)$ . The overall spatial estimation error covariance matrix for any RE  $(f, t)$  is obtained by summing the estimations for all users:

$$\hat{\mathbf{E}}_{f,t} = \sum_{u=1}^{N_k} \hat{\mathbf{E}}_{f,t}^{(k)} \in \mathbb{C}^{N_m \times N_m}. \quad (21)$$

The uplink channel and error covariance estimations are depicted in Fig. 4.

In the downlink, the estimation error variances  $v_{f,t,k}^{(k)}$  and  $v_{f,t,i}^{(k)}$ ,  $i \neq k$  for user  $k$  are estimated following a similar procedure, but with only one receive antenna and using the downlink covariances matrices  $\mathbf{\Omega}$  and  $\mathbf{\Psi}$ . The resulting quantity is denoted by  $\hat{\mathbf{V}}^{(k)}$ , as shown in Fig. 6.

### III. ML-ENHANCED RECEIVER ARCHITECTURE

The baselines presented in the previous section have several limitations. Especially, the NIRE approximation leads to high channel estimation errors for REs that are far from pilots. Similarly, the grouped-equalization can be inaccurate at those REs. This section details the architecture of a receiver that builds on the presented baseline and uses multiple CNNs to improve its performance.

#### A. Receiver training

The ML-enhanced receiver architecture is shown in Fig. 7, where the trainable components are represented in dark grey. In the downlink, each user  $k$  only performs the channel estimation, equalization, and demapping of its own signal, and the corresponding components are illustrated with continuous outlines. However, in the uplink, the BS processes all users in parallel, and the additional components are delimited with dotted lines. Although the internal processing of the trainable components might not be interpretable, using multiple ML-based blocks to perform precise and relatively simple signal processing tasks allows to precisely control which parts of

<sup>2</sup>Similarly to the uplink scenario, this is not true in general.

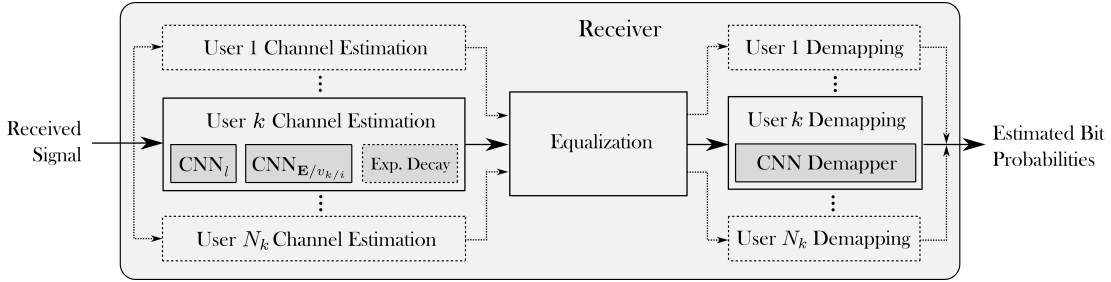


Fig. 7: ML-enhanced receiver architecture. The dotted elements are only present in the uplink, where the BS jointly processes all users. The dark grey elements are trainable components.

the receiver are enhanced. Moreover, this approach makes the output of each ML components easier to interpret, as discussed in Section IV-C for the error statistics  $\hat{\mathbf{E}}$ .

Scalability is achieved by using different copies of the same ML components for every users, where all copies share the same set of trainable parameters. We propose to jointly optimize all these components based only on the estimated bit probabilities, and not by training each of them individually. This approach is practical as it does not assume knowledge of the channel coefficients at training, that can only be estimated through extensive measurement campaigns for practical channels. Let's denote by  $\theta$  the set of trainable parameters of the ML-enhanced receiver, and by  $\hat{b}_{f,t,k,b}$  the sent bit  $(f, t, k, b)$ . In the uplink, those parameters are optimized to minimize the total binary cross-entropy (BCE) :

$$\begin{aligned} \mathcal{L} \triangleq & - \sum_{k=1}^{N_k} \sum_{(f,t) \in \mathcal{D}} \sum_{b=1}^B \mathbb{E}_{\hat{b}, \mathbf{Y}} \left[ \hat{b}_{f,t,k,b} \log_2 \left( \tilde{P}_{\theta}(\hat{b}_{f,t,k,b} = 1 | \mathbf{Y}) \right) \right. \\ & \left. + (1 - \hat{b}_{f,t,k,b}) \log_2 \left( 1 - \tilde{P}_{\theta}(\hat{b}_{f,t,k,b} = 1 | \mathbf{Y}) \right) \right] \end{aligned} \quad (22)$$

where  $\mathcal{D}$  denotes the set of REs carrying data and  $\tilde{P}_{\theta}(\cdot | \mathbf{Y})$  is the receiver estimate of the posterior distribution on the bits given  $\mathbf{Y}$ . The estimated posterior probabilities are obtained by applying the sigmoid function to the corresponding LLRs, i.e.,  $\tilde{P}_{\theta}(\hat{b}_{f,t,k,b} = 1 | \mathbf{Y}) = \text{sigmoid}(\text{LLR}_{f,t,k}(b))$ . In the downlink, the receiver parameters are optimized in a similar manner, except that the signal received by the users is  $\mathbf{R}$ . The expectation in (22) is estimated through Monte Carlo sampling using batches of  $S$  samples :

$$\begin{aligned} \mathcal{L} \approx & - \frac{1}{S} \sum_{s=1}^S \sum_{k=1}^{N_k} \sum_{(f,t) \in \mathcal{D}} \sum_{b=1}^B \left( \hat{b}_{f,t,k,b} \log_2 \left( \tilde{P}_{\theta}(\hat{b}_{f,t,k,b}^{[s]} = 1 | \mathbf{Y}^{[s]}) \right) \right. \\ & \left. + (1 - \hat{b}_{f,t,k,b}) \log_2 \left( 1 - \tilde{P}_{\theta}(\hat{b}_{f,t,k,b}^{[s]} = 1 | \mathbf{Y}^{[s]}) \right) \right) \end{aligned} \quad (23)$$

where the superscript  $[s]$  refers to the  $s^{\text{th}}$  sample in the batch. The loss (22) can be redefined as

$$\mathcal{L} = \sum_{k=1}^{N_k} (\text{Card}(\mathcal{D})B - C_k) \quad (24)$$

where  $\text{Card}(\mathcal{D})$  is the number of REs carrying data and  $\text{Card}(\mathcal{D})M$  is the total number of bits transmitted by one user.

Then, following the derivations available in [21],  $C_k$  can be written as

$$\begin{aligned} C_k = & \sum_{(f,t) \in \mathcal{D}} \sum_{b=1}^B I(\hat{b}_{f,t,k,b}; \mathbf{Y}) \\ & - \sum_{(f,t) \in \mathcal{D}} \sum_{b=1}^B \mathbb{E}_{\mathbf{Y}} \left[ D_{KL} \left( P(\hat{b}_{f,t,k,b} | \mathbf{Y}) || \tilde{P}_{\theta}(\hat{b}_{f,t,k,b} | \mathbf{Y}) \right) \right]. \end{aligned} \quad (25)$$

The first term in (25) is the maximum information rate that can be achieved assuming an ideal bit-metric decoding (BMD) receiver. It depends only on the transmitter and the channel, and therefore acts as a constant during the receiver training. The second term in (25) is the expected value of the KL-divergence between the true posterior probability  $P(\hat{b}_{f,t,k,b} | \mathbf{Y})$  and the one estimated by the proposed receiver. The KL-divergence can be interpreted as a measure of distance between the true and estimated probabilities, which is minimized during training. Moreover,  $C_k$  is an achievable rate for user  $k$  assuming a mismatched BMD receiver [21], meaning that improvements in  $C_k$  directly translate to an improved BER performance.

### B. ML-enhanced channel estimator

As seen in Section II-D, the channel estimation error statistics can only be obtained for REs carrying pilots. However, the estimation accuracy decreases as we move away from them. In the following, we present CNNs that estimate the channel estimation error covariance matrices in the uplink and the estimation error variances in the downlink.

1) *Uplink scenario:* The ML-enhanced uplink channel estimation architecture is depicted in Fig. 9. In this scenario, the spatial channel estimation error covariance matrices  $\mathbf{E}_{f,t}$

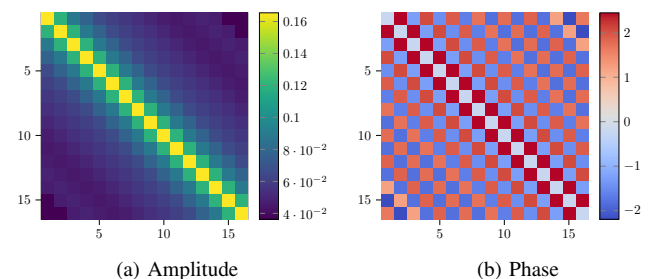


Fig. 8: Example of amplitude and phase for  $\mathbf{E}_{f,t}^{(k)}$ .

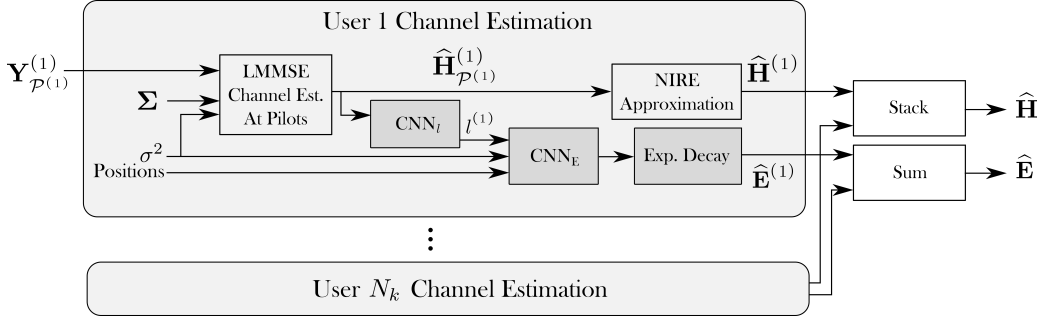


Fig. 9: ML-enhanced uplink channel estimation.

is needed to compute both the equalized symbols (5) and the uplink post-equalization noise variance (9). An example of the amplitude and phase of an estimate of a covariance matrix  $\hat{\mathbf{E}}_{1,1}^{(1)}$  is shown in Fig. 8 for a uniform linear array (ULA) of antennas at the BS. One can see that the amplitude of the coefficients of  $\hat{\mathbf{E}}_{1,1}^{(1)}$  decays rapidly when moving away from the diagonal. The phase, on the other hand, exhibits a more surprising pattern, with a phase difference of roughly  $\pi$  between two adjacent antennas. To predict every element of  $\hat{\mathbf{E}}^{(k)}$  for user  $k$ , a naively designed CNN would need to output  $N_f N_t N_m^2$  complex parameters. This would be of prohibitive complexity for any large number of subcarriers, symbols, or receiving antennas. For this reason, we propose to approximate every element  $(x, y)$  of  $\hat{\mathbf{E}}_{f,t}^{(k)}$  with a complex power decay model:

$$\hat{e}_{f,t,x,y}^{(k)} = \alpha_{f,t} \beta_{f,t}^{|y-x|} \exp(j\gamma(y-x)) \quad (26)$$

where  $y - x$  is the horizontal position difference between that element and the diagonal, and  $\alpha_{f,t}$ ,  $\beta_{f,t}$ , and  $\gamma$  are parameters of this model. For a planar array, one could use such a model for each dimension, and take their Kronecker product to obtain the spatial channel estimation error covariance matrices. A constant phase offset between two adjacent REs is assumed, which matches our experimental observations. The parameters  $\alpha_{f,t}$  and  $\beta_{f,t}$  respectively control the scale and the decay of the model, and depend on the RE  $(f, t)$ .

To estimate those two parameters for each RE, we leverage a

CNN, denoted by  $\text{CNN}_{\mathbf{E}}$ , which takes four inputs, each of size  $N_f \times N_t$ , for a total input dimension of  $N_f \times N_t \times 4$ .  $\text{CNN}_{\mathbf{E}}$  outputs  $\alpha_{f,t}$  and  $\beta_{f,t}$  for every REs, resulting in an output dimension of  $N_f \times N_t \times 2$ . The first two inputs provide the location of every REs in the RG. More precisely, the first input matrix has all columns equal to  $[-\frac{N_f}{2}, \dots, -1, 1, \dots, \frac{N_f}{2}]^T$ , whereas the second one has all rows equal to  $[-\frac{N_t}{2}, \dots, -1, 1, \dots, \frac{N_t}{2}]$ . The third input provides the SNR of the transmission and is given as a matrix  $\text{SNR} \cdot \mathbf{1}_{N_f \times N_t}$ . Finally, the fourth input is a feature  $l^{(k)} \in \mathbb{R}$  provided by another CNN, denoted by  $\text{CNN}_l$ , which was designed with the intuition to predict the time-variability of the channel experienced by user  $k$ . To do so,  $\text{CNN}_l$  uses the channel estimates at REs carrying pilots to estimate the Doppler and delay spread. Although we cannot be certain that  $\text{CNN}_l$  effectively learns to extract such information, the evaluations presented in Section IV-C tend to support this hypothesis.  $\text{CNN}_l$  takes an input of dimension  $N_{P_f} \times N_{P_t} \times 2N_m$ , which corresponds to the stacking of the real and imaginary parts of  $\hat{\mathbf{H}}_{\mathcal{P}^{(k)}}^{(k)}$  along the last dimension. It outputs the scalar  $l^{(k)}$ , which is fed to  $\text{CNN}_{\mathbf{E}}$  as the matrix  $l^{(k)} \cdot \mathbf{1}_{N_f \times N_t}$ .

2) *Downlink scenario*: In the downlink, the equivalent channel estimation error variances  $\mathbf{V}^{(k)}$  are needed to compute  $\tau_{f,t,k}^2$  in (17). To estimate those variances, we take inspiration from the architecture presented in Section II which uses two different downlink covariance matrices  $\mathbf{\Omega}$  and  $\mathbf{\Psi}$  to estimate the error variances of the main and interfering channels.

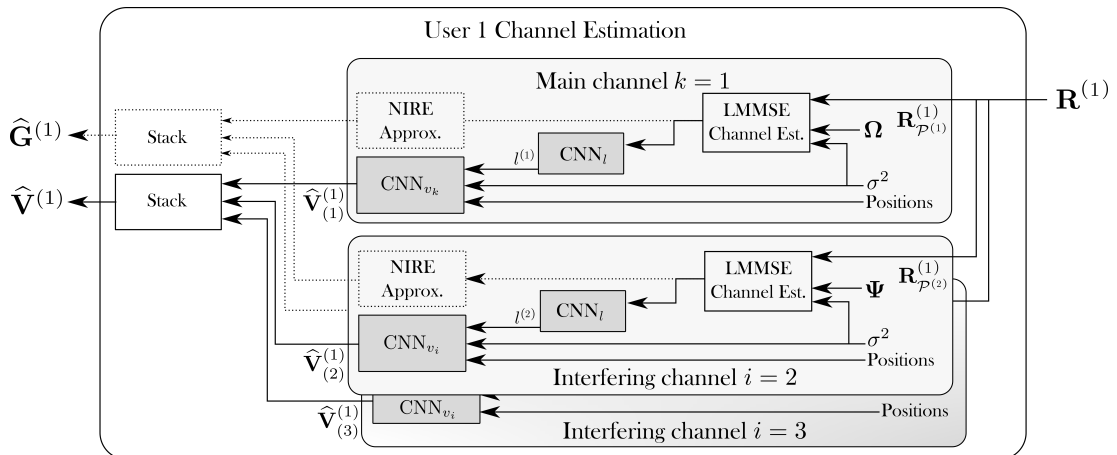
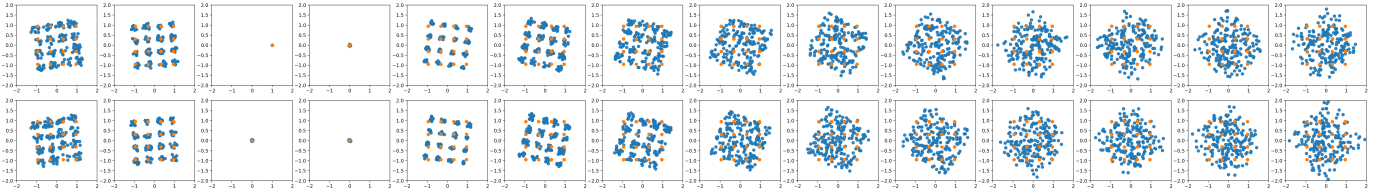
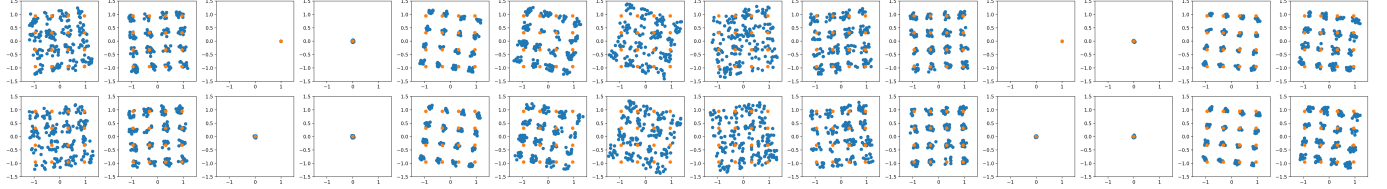


Fig. 10: Detailed view of the downlink *Channel Estimation* component of user 1 out of  $N_k = 3$ , as depicted in Fig 6.



(a) IP pilot pattern.



(b) 2P pilot pattern.

Fig. 11: Mismatch between the sent signals (orange) and the equalized received ones (blue) for a single user out of four and using 16-QAM modulation.

Similarly, we leverage two separate CNNs, denoted by  $\text{CNN}_{v_k}$  and by  $\text{CNN}_{v_i}$ , to respectively predict the estimation error variances of the main channel  $\hat{v}_{f,t,k}^{(k)}$  and of an interfering channel  $\hat{v}_{f,t,i}^{(k)}$ ,  $i \neq k$ . Both CNNs take the same inputs as  $\text{CNN}_E$  but their outputs are of dimension  $N_f \times N_t$  as variances are predicted for all REs ( $f, t$ ). To preserve the scalability of the conventional architecture,  $N_k - 1$  copies of  $\text{CNN}_{v_i}$  are leveraged to estimate the error variances  $\hat{v}_{f,t,i}^{(k)}$  of all  $N_k - 1$  interferers. The downlink channel estimation is schematically shown in Fig. 10, where  $\hat{\mathbf{V}}_{(a)}^{(k)} = \{\hat{v}_{f,t,a}^{(k)}\}_{(f,t) \in \{0, \dots, N_f\} \times \{0, \dots, N_t\}}$  denotes the estimation error variances seen by user  $k$  on its main or interfering channel  $a$ .

### C. ML-enhanced demapper

A consequence of unperfect channel estimation and equalization is channel aging, which leads to residual distortion on the equalized signals, as illustrated in Fig. 11. The signals sent by a single user out of four are represented in orange, while the corresponding equalized received signals are shown in blue, assuming spectral channel interpolation only. This figure has been obtained by sending a large batch of signals using a fixed realization of a fast-varying channel, and only displays the first two subcarriers of the uplink slot. Moreover, an infinite SNR is assumed so that only the effects of channel aging and interference are visible. One can see that the equalized symbols suffer from little distortion and interference

at REs close to the pilots, but these unwanted effects become increasingly stronger at REs that are away from them.

A traditional demapper, as presented in Section II-B3, operates independently on each RE and therefore only sees one equalized symbol at a time. In contrast, we propose to use a CNN, called  $\text{CNN}_{\text{Dmp}}$ , to perform a joint demapping of the entire RG. By jointly processing all equalized symbols, the CNN can estimate and correct the effects of channel aging to compute better LLRs. The input of  $\text{CNN}_{\text{Dmp}}$  is of dimension  $N_f \times N_t \times 6$  and carries the subcarriers and symbol indices for each RE, the SNR, the real and imaginary parts of the equalized symbols, and the post-equalization channel noise variances. The output of  $\text{CNN}_{\text{Dmp}}$  has dimensions  $N_f \times N_t \times M$  and corresponds to the predicted LLRs<sup>(k)</sup> over the RG for a user  $k$ . As with a conventional receiver, the demapping is performed independently for each user to make the architecture easily scalable. The  $\text{CNN}_{\text{Dmp}}$  demapper is shown in Fig. 12, which depicts the uplink demapping process.

### D. CNN architectures

All CNNs presented above share the same building blocks: convolutional 2D layers, dense layers, and custom ResNet layers. The custom ResNet layers, inspired by [31], consist of a batch normalization layer, a rectified linear unit (ReLU), a 2D separable convolutional layer, and finally the addition of the input, as depicted in Fig. 13. Separable convolutions are less computationally expensive while maintaining similar

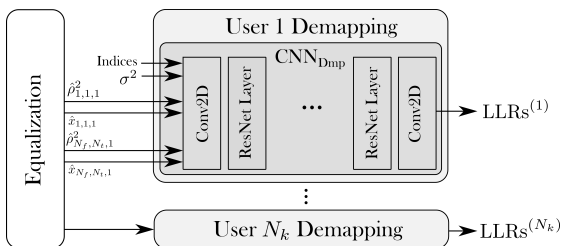


Fig. 12: Uplink demapping using the CNN-based demapper.

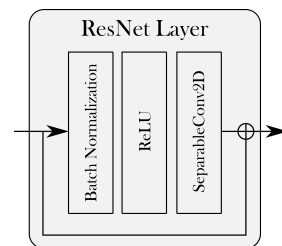


Fig. 13: Custom ResNet layer.

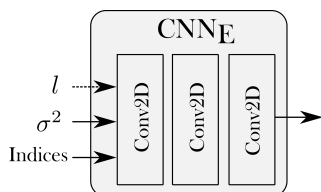
	CNN <sub>E</sub> /CNN <sub>v<sub>k,i</sub></sub>				CNN <sub>l</sub>				CNN <sub>Dmp</sub>			
	$N_f \times N_k \times 4$				$N_{P_f} \times N_{P_t} \times 2N_m$				$N_f \times N_k \times 6$			
Input size	filters	kernel	dilat.	act.	filters	kernel	dilat.	act.	filters	kernel	dilat.	act.
Conv2D	32	(5,3)	(1,1)	ReLU	32	(1,1)	(1,1)	-	128	(1,1)	(1,1)	-
ResNet Layer	-				32	(3,2)	(1,1)	-	128	(3,3)	(1,1)	-
ResNet Layer	-				32	(5,2)	(2,1)	-	128	(5,3)	(2,1)	-
ResNet Layer	-				32	(7,2)	(3,1)	-	128	(7,3)	(3,2)	-
ResNet Layer	-				32	(5,2)	(2,1)	-	128	(9,3)	(4,3)	-
ResNet Layer	-				32	(3,2)	(1,1)	-	128	(7,3)	(3,2)	-
ResNet Layer	-				-				128	(5,3)	(2,1)	-
ResNet Layer	-				-				128	(3,3)	(1,1)	-
Conv2D	32	(5,3)	(1,1)	ReLU	1	(3,2)	(1,1)	-	$M$	(1,1)	(1,1)	-
Conv2D	2 / 1	(1,1)	(1,1)	Sigm.	-				-			
Output Layer	-				Dense, units = 1				-			
Output size	$N_f \times N_k \times 2/N_f \times N_k \times 1$				1				$N_f \times N_k \times M$			

TABLE I: Parameters of the different CNNs.

performance as regular convolutional layers [32]. CNN<sub>E</sub>, CNN<sub>v<sub>k</sub></sub>, and CNN<sub>v<sub>i</sub></sub> are all made of three 2D convolutional layers, as shown in Fig.14 for CNN<sub>E</sub>. The first two layers are followed by a ReLU activation function, while the last layer is followed by a sigmoid activation function. CNN<sub>Dmp</sub> and CNN<sub>l</sub> also share a similar architecture, depicted in Fig.12 and Fig 15, respectively. Both are composed of a 2D convolutional layer, followed by multiple ResNet layers and a 2D convolutional layer. CNN<sub>l</sub> outputs a single scalar, which is ensured by using a dense layer with a single unit and no activation function as output layer. Inspired by [12], we used increasing followed by decreasing kernel sizes and dilation rates to increase the receptive field of the CNN. All convolutional and separable convolutional layers use zero-padding so that the output dimensions matches the input dimensions. Details of the architectures of all CNNs are given in Table I.

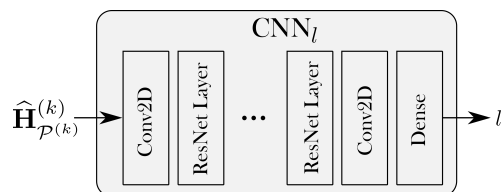
#### IV. EVALUATIONS

In this section, the proposed ML-enhanced receiver is evaluated and compared against two baselines: the one presented in Section II as well as a perfect CSI baseline that will be detailed later on. The training and evaluation setups are first introduced, followed by a numerical evaluation of the uplink and downlink performance for the 1P and 2P pilot patterns from Fig. 2.

Fig. 14: Architecture of CNN<sub>E</sub>.

#### A. Training and evaluation setup

For realistic training and evaluation, the channel realizations were generated with QuaDRiGa version 2.0.0 [33]. It has been experimentally observed in [12] that a receiver trained on certain scenarios was able to generalize to other channel models. For this reason, we only focus on the 3GPP non-line of sight (NLOS) urban microcell (UMi) scenario [34]. The number of users was set to  $N_k = 4$ , except for the downlink at high speeds where it was reduced to  $N_k = 2$ , and the number of antennas at the BS was set to  $N_m = 16$ . All users were randomly placed within a 120° cell sector, with a minimum distance of 15 m and a maximum distance of 150 m from the BS. The user and BS heights were respectively set to 1.5 m and 10 m. The RGs were composed of six resource blocks for a total of  $N_f = 72$  subcarriers, with a center frequency of 3.5 GHz and a subcarrier spacing of 15 kHz. Both the uplink and downlink slots contained  $N_t = 14$  OFDM symbols. A Gray-labeled QAM was used with  $M = 4$  bits per channel use on the uplink and  $M = 2$  bits per channel use on the downlink. The receivers were trained and evaluated on users moving at independent random speeds. Three ranges of low speeds were considered with the 1P pilot pattern : 0 to 15 km h<sup>-1</sup>, 15 to 30 km h<sup>-1</sup>, and 30 to 45 km h<sup>-1</sup>. Similarly, three high speed ranges were considered with the 2P pilot pattern : 50 to 70 km h<sup>-1</sup>, 80 to 100 km h<sup>-1</sup>, and 110 to 130 km h<sup>-1</sup>. We noticed that CNN<sub>l</sub> was not able to extract useful information when using the 1P pattern, and therefore was not used in the

Fig. 15: Architecture of CNN<sub>l</sub>.

Parameters	Symbol (if any)	Value
Number of users	$N_k$	4 (2 in high speed downlink)
Number of antennas at the BS	$N_m$	16
Number of subcarrier	$N_f$	72 = 6 resource blocks
Number of OFDM symbols	$N_t$	14 (uplink) + 14 (downlink)
Bit per channel use	$B$	4 bit (uplink), 2 bit(downlink)
Center frequency	-	3.5 GHz
Subcarrier spacing	-	15 kHz
Scenario	-	3GPP 38.901 UMi NLOS
Code length	-	1296 bit
Code rate	$\eta$	$\frac{1}{2}$ (uplink), $\frac{1}{3}$ (downlink)
Learning rate	-	$10^{-3}$
Batch size	$S$	27 RGs

TABLE II: Training and evaluation parameters.

corresponding trainings and evaluations. For equalization, the grouped-LMMSE equalizer operated on groups of  $2 \times 7$  REs, following the segmentation delimited by the thick black line of the 2P pattern, shown in Fig. 2c. The training and evaluation parameters are provided in Table II.

Separate training sets were constructed for the 1P and 2P pilot pattern, both made of channel realizations corresponding to 1000 RGs of each respective user speed range, for a total of 3000 RGs per training dataset. Evaluations were performed separately for each user speed range with datasets containing 3000 RGs and a standard IEEE 802.11n low-density parity-check (LDPC) code of length 1296 bit [35]. Code rates of  $\frac{1}{2}$  and  $\frac{1}{3}$  were used respectively for uplink and downlink transmissions. Decoding was done with 40 iterations using a conventional belief-propagation decoder. To satisfy the perfect power assumption in (1), each RG was normalized to have an average energy of one per antenna and per user:

$$\sum_{f=1}^{N_f} \sum_{t=1}^{2N_t} \|\mathbf{h}_{f,t}^{(k)}\|_2^2 = N_f 2N_t N_m. \quad (27)$$

Each training was carried out using batches of size  $S = 27$  so that the total number of bits sent for each user was a multiple of the code length. The trainable parameters  $\theta$  were all initialized randomly except for  $\gamma$  in (26) that was initialized with  $\pi$ . Training was done through stochastic gradient descent (SGD) using the Adam [36] optimizer and a learning rate of  $10^{-3}$ . The best performing random initialization out of ten was selected.

### B. Uplink simulation results

Different schemes were benchmarked in the uplink simulations. The first one is the uplink baseline presented in Sections II-B and II-D. The second one, named ‘ML channel estimator’, leverages the ML-enhanced channel estimator presented in III-B1 but is trained and tested with a standard demapper. The third one is the ML-enhanced receiver, leveraging both the enhanced channel estimator and demapper. We refer to it as ‘ML receiver’. Evaluating the ML channel

estimator separately allows us to better understand the role both components play in the observed gains. An ideal baseline with perfect knowledge of the channel at the REs carrying pilots and of  $\mathbf{E}$  is also considered, and referred to as ‘Perfect CSI’. All schemes used spectral interpolation followed by NIRE approximation for channel estimation. Additional simulations were conducted for the 2P pilot pattern using spectral and temporal interpolation for both the baseline and the ML receiver. Finally, an ML receiver trained with only  $N_k = 2$  users was also evaluated.

Simulation results for the 1P pattern are shown in the first row of Fig. 16 for the three different speed ranges. At speeds ranging from 0 to  $15 \text{ km h}^{-1}$ , one can see that the ML channel estimator does not bring any improvements, whereas the ML receiver achieves a 1 dB gain at a coded BER of  $10^{-3}$ . The benefit of having a better estimation of  $\mathbf{E}$  becomes more significant as the speed increases. At the highest speed range (Fig. 16c), the ML receiver enables gains of 3 dB over the baseline at a coded BER of  $10^{-2}$ . It can be observed that the ML receiver trained with only two users nearly matches the performance of the one trained with four users on all considered speeds, demonstrating the scalability of the proposed scheme with respect to the number of users.

Results for the 2P pilot pattern are shown in the second row of Fig. 16. The gains provided by the ML channel estimator alone and by the entire ML receiver follow the same trend as with the 1P pattern, with moderate gains at  $50\text{-}70 \text{ km h}^{-1}$ , but significant improvements at  $110\text{-}130 \text{ km h}^{-1}$ . More precisely, the ML receiver provides a 1 dB gain over the baseline at a coded BER of  $10^{-3}$  in the  $50\text{-}70 \text{ km h}^{-1}$  range, and is the only scheme that achieves a coded BER of  $10^{-3}$  for the highest speeds with spectral interpolation only. Indeed, at high speeds, the learned demapper is still able to mitigate the effects of channel aging, whereas even the perfect CSI baseline suffers from strongly distorted equalized signals. Using both spectral and temporal interpolations reduces the gains provided by the ML receiver, which can be explained by the better channel estimates leading to less channel aging, but they still amount to a 2.2 dB gap at a BER of  $10^{-3}$  for the highest speeds. We have

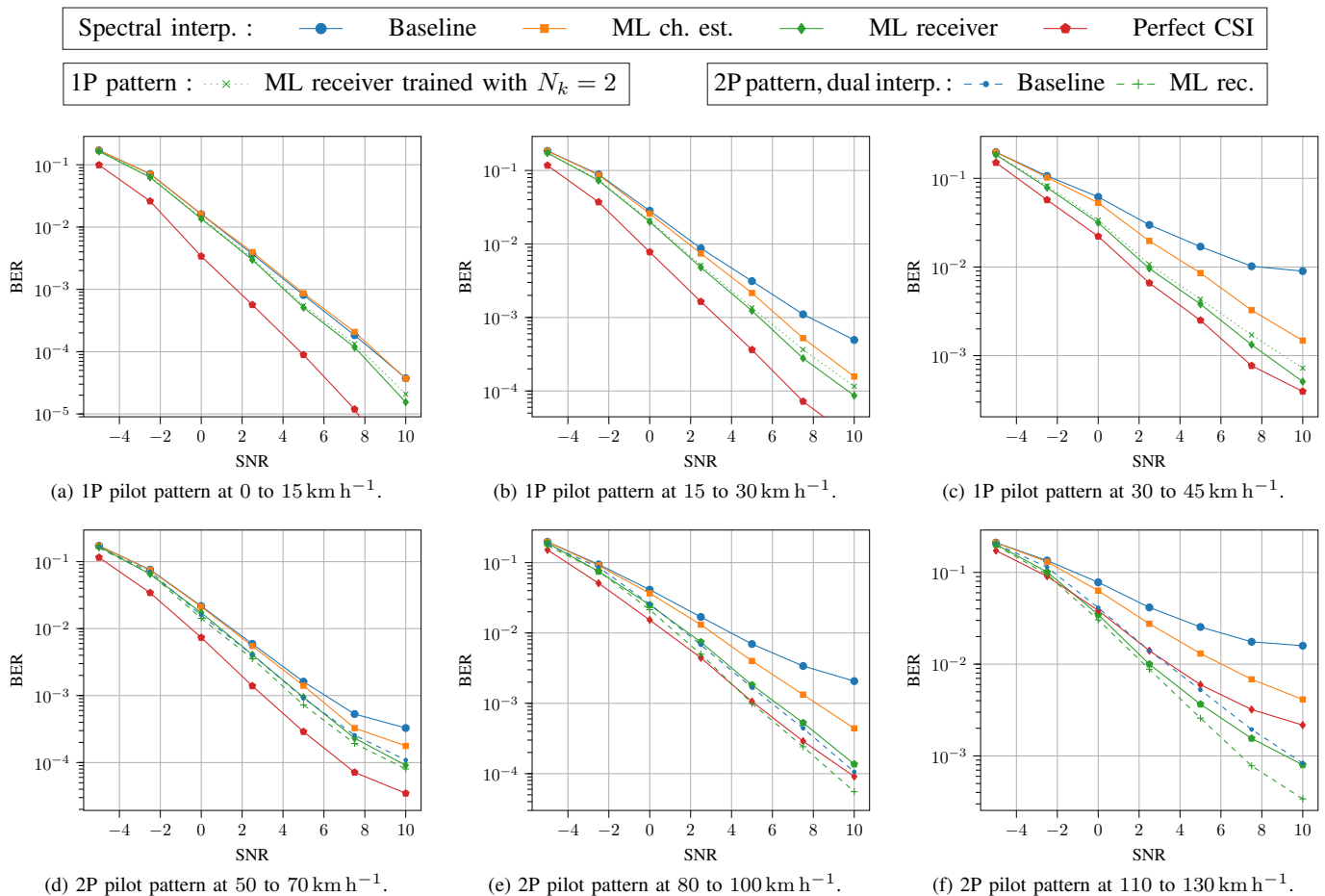


Fig. 16: Uplink BER achieved by the different receivers with the 1P and 2P pilot patterns.

also experimentally verified that an ML receiver trained with only  $N_k = 2$  users was able to closely match the performance of the one trained with  $N_k = 4$ , but decided not to include the corresponding curves for clarity reasons. Overall, one can see that only the combination of a CNN-based estimation of the channel estimation error statistics and CNN-based demapper enables gains for both pilot patterns and all speed ranges.

### C. Visualizing the channel estimation error statistics

In order to get insights into the ML channel estimator abilities, we visualize the channel estimation error covariance matrices  $\mathbf{E}$  for different user speeds. Two batches of uplink signals were sent, with users respectively moving at  $60 \text{ km h}^{-1}$  and  $120 \text{ km h}^{-1}$ . All batches comprised 90 RGs, and leveraged the 2P pilot pattern with an SNR of 5 dB. The Frobenius norms corresponding to each REs'  $\|\mathbf{E}_{f,t}\|_F$  are shown in Fig. 17, and the normalized errors  $\left| \frac{\|\hat{\mathbf{E}}_{f,t}\|_F - \|\mathbf{E}_{f,t}\|_F}{\|\mathbf{E}_{f,t}\|_F} \right|$  are shown in Fig. 18. The figures labeled as ‘Predicted’ refers to the estimations  $\hat{\mathbf{E}}_{f,t}$  produced by the ML channel estimator and averaged over the corresponding batches, using spectral interpolation only. As expected, the Frobenius norms of the REs carrying data strongly depend on their distance to their closest pilot, reflecting the distortions visible in Fig. 11b. The figures labeled as ‘True’ are presented for reference, and are computed by

Monte Carlo simulations assuming knowledge of the true channel realizations. One can see that the normalized errors are low on REs carrying data, confirming that  $\text{CNN}_{\mathbf{E}}$  is able to learn the channel estimation error statistics from the data during training. The higher errors on REs carrying pilots are due to the loss (23) taking solely into account the positions  $(f, t) \in \mathcal{D}$ , giving no opportunities for  $\text{CNN}_{\mathbf{E}}$  to learn the statistics at pilot positions. Experiments conducted using both spectral and temporal interpolation yielded higher normalized errors, probably because the increased accuracy of the channel estimates results in a more difficult learning of the error statistics. Additionally,  $\text{CNN}_l$  seems to correctly estimate the time-variability of the channels since the Frobenius norms of the predicted covariances increase with the user speed, matching the behavior of the true covariances.

It is also insightful to look at the predicted and true spatial covariance matrix for a single RE. We chose to focus on the RE (36, 7), positioned at the center of the OFDM grid, and on the  $120 \text{ km h}^{-1}$  scenario (Fig. 17b). The amplitudes and phases of all elements of  $\hat{\mathbf{E}}_{36,7}$  and  $\mathbf{E}_{36,7}$  are shown in Fig. 19a and 19b. One can see that the predicted amplitudes and phases are close to the true ones, thus supporting the proposed power decay model.

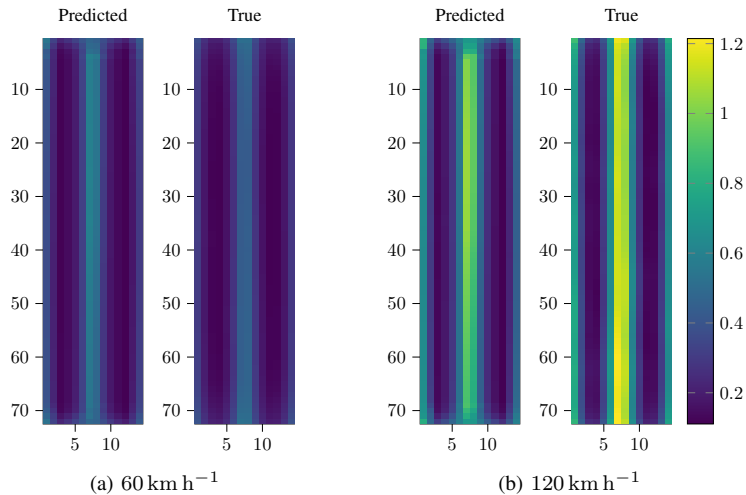


Fig. 17:  $\|\widehat{\mathbf{E}}_{f,t}\|_F$  vs  $\|\mathbf{E}_{f,t}\|_F$  for different user speeds.

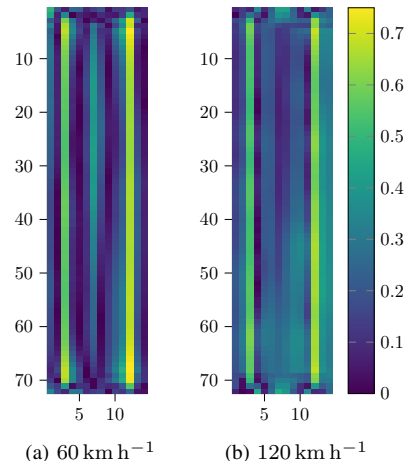


Fig. 18: Normalized error.

#### D. Downlink simulation results

Four downlink schemes were evaluated on the considered speed ranges. The first one is the baseline presented in Section II. In the second one, referred to as ‘ML channel estimator’, each user leverages the enhanced channel estimator of Section III-B2 and is trained and tested with a standard demapper. The third one is the ML-enhanced receiver using both the enhanced channel estimator and ML demapper for each user, and is referred to as ‘ML receiver’. The last scheme has perfect CSI, i.e., all users perfectly know both the channel at REs carrying pilots and the estimation error variances  $v_{f,t,k}^{(k)}$  and  $v_{f,t,i}^{(k)}$  everywhere. All schemes use the 2P pilot pattern to perform the uplink channel estimation, but are evaluated on both patterns in the downlink. Similarly to the uplink, all schemes leveraged spectral interpolation with NIRE approximation for channel estimation, but additional simulations were performed with the 2P pilot pattern using spectral and temporal interpolation for both the baseline and the ML receiver. An ML receiver trained with only  $N_k = 2$  users was also evaluated on the three slowest speed ranges.

The 1P pilot pattern downlink evaluations are shown in the first row of Fig. 20. Between 0 and 15 km h<sup>-1</sup>, all schemes achieve good results but the ML receivers are the only ones to not saturate at high SNRs. As expected, the gains allowed by the learned channel estimator and demapper increase with

the speed, and the ML receiver is the only scheme to reach a BER of approximately  $10^{-3}$  in the 30-45 km h<sup>-1</sup> speed range. It can also be observed that the ML receiver trained with only  $N_k = 2$  users is able to closely match the performance of the ML receiver trained with four users. The 2P pilot pattern evaluations are shown in the second row of Fig. 20 for higher speeds. In this new setup, the ML receiver outperforms the baseline by 1.1 dB at a BER of  $10^{-3}$  in the speed range 50-70 km h<sup>-1</sup>, and is the only one with spectral interpolation only to achieve a BER of  $10^{-3}$  in the speed range 70-90 km h<sup>-1</sup>. Using both spectral and temporal interpolations, the ML receiver still provides significant gains at high speeds, being the only one to achieve a BER of  $10^{-3}$  in the 110-130 km h<sup>-1</sup> speed range.

In all downlink scenarios except for the slowest speed range, the ML channel estimator outperforms the perfect CSI baseline. This can be surprising since this baseline uses the exact noise variances  $v_{f,t,k}^{(k)}$  and  $v_{f,t,i}^{(k)}$  while the ML schemes can only estimate them. We suppose that this is because the baselines assume that the noise  $o_{f,t,k}$  in (16) is Gaussian distributed and uncorrelated to the transmitted signal, which is typically untrue. The ML channel estimator seems able to learn this model mismatch during training and predict variances that counteract it.

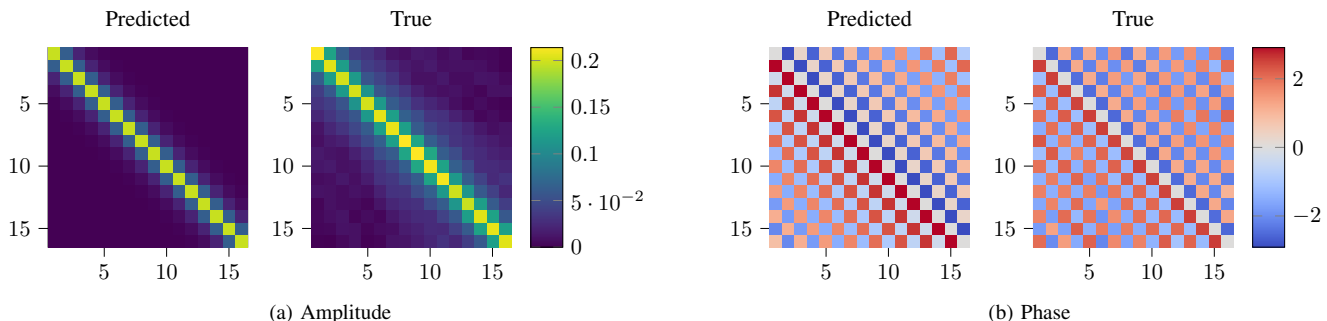


Fig. 19: Amplitude and phase of  $\widehat{\mathbf{E}}_{36,7}$  and  $\mathbf{E}_{36,7}$  for a single channel realization at 120 km h<sup>-1</sup>.

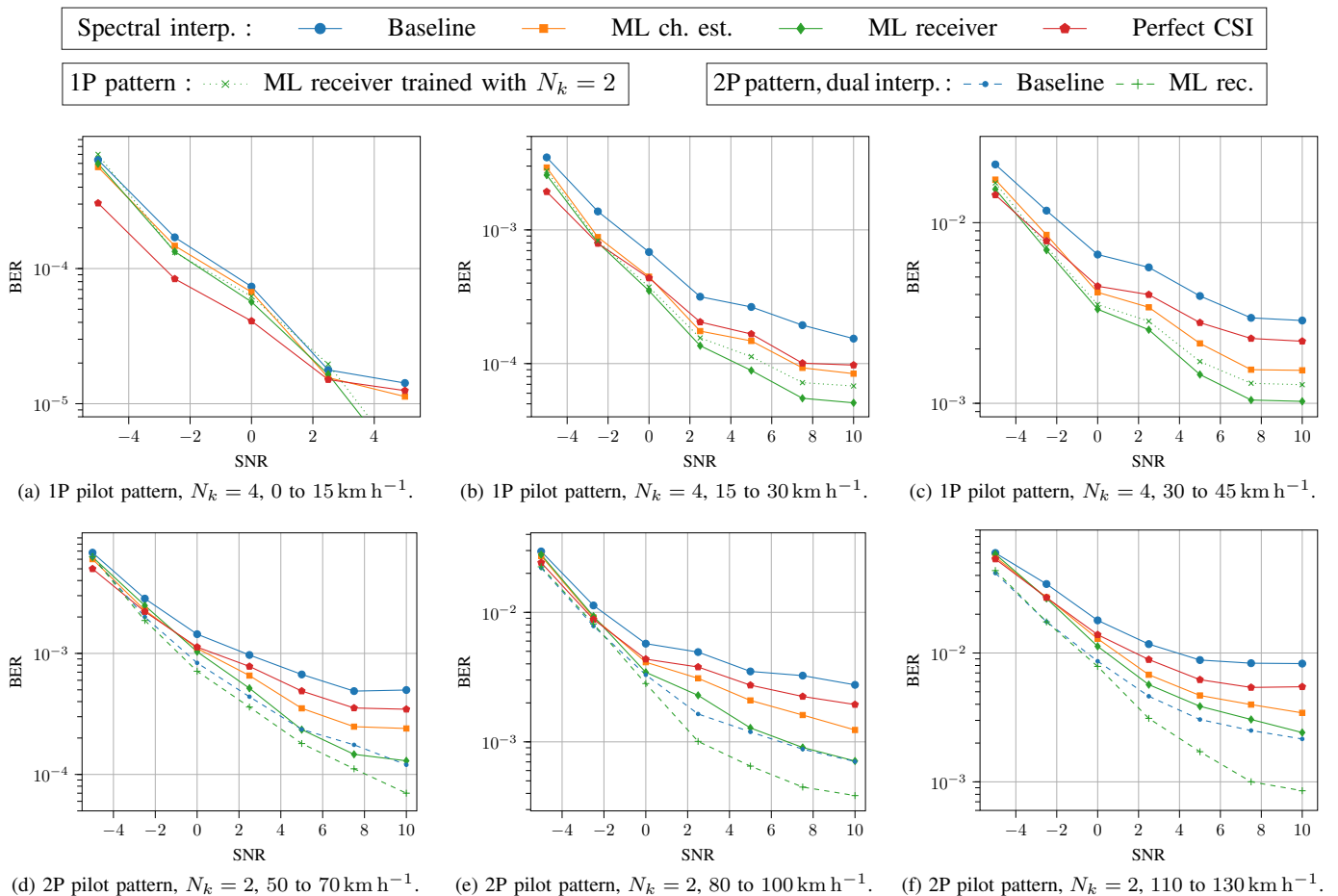


Fig. 20: Downlink BER achieved by the different receivers with the 1P and 2P pilot patterns.

## V. CONCLUSION

We propose in this paper a MU-MIMO receiver that builds on top of a traditional receiver architecture and enhances it with ML components. More precisely, CNNs are leveraged to improve both the demapping and the computation of the channel estimation error statistics. All components of the proposed architecture are jointly optimized to refine the estimation of the LLRs. This approach does not require any knowledge of the channel for training, is interpretable, and easily scalable to any number of users. Uplink and downlink evaluations were performed with multiple user speeds and two different pilot configurations on 3GPP-compliant channel models. The results reveal that the proposed architecture effectively exploits the OFDM structure to achieve tangible gains at low speeds and significant ones at high speeds compared to a traditional receiver. On the one hand, the enhanced demapper jointly processes all REs of the OFDM grid to counteract the effects of channel aging. On the other hand, we demonstrated that the enhanced channel estimator is able to learn its error statistics during training. In order to get insights into the improvements enabled by each of the trainable components, we also evaluated a conventional structure where only the channel estimator was enhanced. The results indicate that the combined use of both the ML channel estimator and demapper is key to achieve a substantial reduction of the coded BERs across all scenarios.

Possible research directions include a more detailed study of the adaptability of the proposed architecture to any number of users, and enhancements to other parts of the receiver such as the equalization or the estimation of the channel coefficients. We have also observed that further gains can be enabled by jointly processing all users as in [10]. However, unlocking these gains while preserving the flexibility and interpretability of conventional architectures is a significant challenge that is yet to be solved.

## APPENDIX

### A. Grouped-LMMSE equalizer

We aim to find the LMMSE matrix to equalize a group of REs that spans multiple subcarriers  $f \in [F_b, F_e]$  and symbols  $t \in [T_b, T_e]$ , with  $1 \leq F_b \leq F_e \leq N_f$  and  $1 \leq T_b \leq T_e \leq N_t$ . Let us denote by  $\hat{\mathbf{H}}_{f,t}$  the channel estimated at a RE  $(f, t)$  and by  $\tilde{\mathbf{H}}_{f,t}$  the corresponding estimation errors. It is assumed that  $\hat{\mathbf{H}}$  is known, but that  $\mathbf{H}$ , the symbols, and the noise, conditioned on the channel estimates, are random and uncorrelated. The channel transfer function for that group is

$$\mathbf{y}_{f,t} = \left( \hat{\mathbf{H}}_{f,t} + \tilde{\mathbf{H}}_{f,t} \right) \mathbf{x}_{f,t} + \mathbf{n}_{f,t}. \quad (28)$$

We denote by  $\mathbf{W}_{f,t}$ ,  $f \in [F_b, F_e]$ ,  $t \in [T_b, T_e]$ , the LMMSE matrix that minimizes

$$\begin{aligned}\mathcal{L}(\mathbf{W}_{f,t}) &= \sum_{f'=F_b}^{F_e} \sum_{t'=T_b}^{T_e} \text{MSE}(\mathbf{x}_{f',t'}, \mathbf{W}_{f,t} \mathbf{y}_{f',t'}) \\ &= \mathbb{E} \left[ \sum_{f'=F_b}^{F_e} \sum_{t'=T_b}^{T_e} (\mathbf{x}_{f',t'} - \mathbf{W}_{f,t} \mathbf{y}_{f',t'}) (\mathbf{x}_{f',t'} - \mathbf{W}_{f,t} \mathbf{y}_{f',t'})^H \right].\end{aligned}\quad (29)$$

Therefore,  $\mathbf{W}_{f,t}$  nulls the gradient

$$\begin{aligned}\nabla \mathbf{w}_{f,t} \mathcal{L}(\mathbf{W}_{f,t}) &= 2\mathbf{W} \mathbb{E} \left[ \sum_{f'=F_b}^{F_e} \sum_{t'=T_b}^{T_e} \mathbf{y}_{f',t'} \mathbf{y}_{f',t'}^H \right] \\ &\quad - 2\mathbb{E} \left[ \sum_{f'=F_b}^{F_e} \sum_{t'=T_b}^{T_e} \mathbf{x}_{f',t'} \mathbf{y}_{f',t'}^H \right] \stackrel{!}{=} 0\end{aligned}\quad (30)$$

which leads to

$$\mathbf{W}_{f,t} = \left( \mathbb{E} \left[ \sum_{f'=F_b}^{F_e} \sum_{t'=T_b}^{T_e} \mathbf{x}_{f',t'} \mathbf{y}_{f',t'}^H \right] \right) \quad (31)$$

$$\begin{aligned}&\left( \mathbb{E} \left[ \sum_{f'=F_b}^{F_e} \sum_{t'=T_b}^{T_e} \mathbf{y}_{f',t'} \mathbf{y}_{f',t'}^H \right] \right)^{-1} \\ &= \left( \sum_{f'=F_b}^{F_e} \sum_{t'=T_b}^{T_e} \hat{\mathbf{H}}_{f',t'}^H \right) \quad (32) \\ &\left( \sum_{f'=F_b}^{F_e} \sum_{t'=T_b}^{T_e} \left( \hat{\mathbf{H}}_{f',t'} \hat{\mathbf{H}}_{f',t'}^H + \mathbb{E} \left[ \tilde{\mathbf{H}}_{f',t'} \tilde{\mathbf{H}}_{f',t'}^H \right] + \sigma^2 \mathbf{I}_{N_m} \right) \right)^{-1}.\end{aligned}$$

## REFERENCES

- [1] T. O'Shea and J. Hoydis, "An Introduction to Deep Learning for the Physical Layer," *IEEE Trans. Cogn. Commun. Netw.*, vol. 3, no. 4, pp. 563–575, 2017.
- [2] E. Nachmani, Y. Be'ery, and D. Burshtein, "Learning to Decode Linear Codes Using Deep Learning," in *Annu. Allerton Conf. on Commun., Control, and Comput.*, 2016, pp. 341–346.
- [3] H. Sun, X. Chen, Q. Shi, M. Hong, X. Fu, and N. D. Sidiropoulos, "Learning to Optimize: Training Deep Neural Networks for Wireless Resource Management," in *Proc. IEEE Int. Workshop Signal Process. Adv. Wireless Commun. (SPAWC)*, 2017.
- [4] D. Gündüz, P. de Kerret, N. D. Sidiropoulos, D. Gesbert, C. R. Murthy, and M. van der Schar, "Machine Learning in the Air," *IEEE J. Sel. Areas Commun.*, vol. 37, no. 10, pp. 2184–2199, 2019.
- [5] S. Dörner, S. Cammerer, J. Hoydis, and S. t. Brink, "Deep Learning Based Communication Over the Air," *IEEE J. Sel. Topics Signal Process.*, vol. 12, no. 1, pp. 132–143, 2018.
- [6] J. Downey, B. Hilburn, T. O'Shea, and N. West, "Machine learning remakes radio," *IEEE Spectrum*, vol. 57, no. 5, 2020.
- [7] E. Björnson, J. Hoydis, and L. Sanguinetti, "Massive MIMO Networks: Spectral, Energy, and Hardware Efficiency," *Found. and Trends® in Signal Proc.*, vol. 11, no. 3-4, pp. 154–655, 2017. [Online]. Available: <http://dx.doi.org/10.1561/20000000093>
- [8] S. Yang and L. Hanzo, "Fifty years of mimo detection: The road to large-scale mimos," *IEEE Commun. Surveys Tuts.*, vol. 17, no. 4, pp. 1941–1988, 2015.
- [9] K. Pratik, B. D. Rao, and M. Welling, "RE-MIMO: Recurrent and Permutation Equivariant Neural MIMO Detection," *preprint arXiv:2007.00140*, 2020.
- [10] D. Korpi, M. Honkala, J. M. J. Huttunen, and V. Starck, "DeepRx MIMO: Convolutional MIMO Detection with Learned Multiplicative Transformations," *preprint arXiv:2010.16283*, 2020.
- [11] P. Dong, H. Zhang, G. Y. Li, I. S. Gaspar, and N. NaderiAlizadeh, "Deep CNN-Based Channel Estimation for mmWave Massive MIMO Systems," *IEEE J. Sel. Topics Signal Process.*, vol. 13, no. 5, pp. 989–1000, 2019.
- [12] M. Honkala, D. Korpi, and J. M. J. Huttunen, "DeepRx: Fully Convolutional Deep Learning Receiver," *preprint arXiv:2005.01494*, 2020.
- [13] S. Cammerer, F. A. Aoudia, S. Dörner, M. Stark, J. Hoydis, and S. ten Brink, "Trainable Communication Systems: Concepts and Prototype," *IEEE Trans. Commun.*, vol. 68, no. 9, pp. 5489–5503, 2020.
- [14] N. Samuel, T. Diskin, and A. Wiesel, "Learning to Detect," *IEEE Trans. Signal Process.*, vol. 67, no. 10, 2019.
- [15] H. He, C. Wen, S. Jin, and G. Y. Li, "A Model-Driven Deep Learning Network for MIMO Detection," in *Proc. IEEE Global Conf. Signal Inf. Process. (GlobalSIP)*, 2018, pp. 584–588.
- [16] M. Khani, M. Alizadeh, J. Hoydis, and P. Fleming, "Adaptive Neural Signal Detection for Massive MIMO," *IEEE Trans. Wireless Commun.*, vol. 19, no. 8, pp. 5635–5648, 2020.
- [17] M. Goutay, F. A. Aoudia, and J. Hoydis, "Deep HyperNetwork-Based MIMO Detection," *preprint arXiv:2002.02750*, 2020.
- [18] D. Neumann, T. Wiese, and W. Utschick, "Learning the MMSE Channel Estimator," *IEEE Trans. Signal Process.*, vol. 66, no. 11, pp. 2905–2917, 2018.
- [19] M. B. Mashhadi and D. Gunduz, "Pruning the Pilots: Deep Learning-Based Pilot Design and Channel Estimation for MIMO-OFDM Systems," *preprint arXiv:2006.11796*, 2020.
- [20] O. Shental and J. Hoydis, "'Machine LLRning': Learning to Softly Demodulate," *preprint arXiv:1907.01512*, 2020.
- [21] F. Ait Aoudia and J. Hoydis, "End-to-end Learning for OFDM: From Neural Receivers to Pilotless Communication," *preprint arXiv:2009.05261*, 2020.
- [22] A. Öztekin and E. Ergelebi, "An efficient soft demapper for APSK signals using extreme learning machine," *Neural Comput. Appl.*, vol. 31, no. 10, pp. 5715–5727, 2019.
- [23] M. Schaedler, G. Boecherer, and S. Pachnicke, "Soft-Demapping for Short Reach Optical Communication: A Comparison of Deep Neural Networks and Volterra Series," *J. Lightw. Technol.*, 2021.
- [24] H. Ye, G. Y. Li, and B. Juang, "Power of Deep Learning for Channel Estimation and Signal Detection in OFDM Systems," *IEEE Wireless Commun. Lett.*, vol. 7, no. 1, pp. 114–117, 2018.
- [25] Z. Zhao, M. C. Vuran, F. Guo, and S. Scott, "Deep-Waveform: A Learned OFDM Receiver Based on Deep Complex Convolutional Networks," *preprint arXiv:1810.07181*, 2018.
- [26] Y. Zhang, A. Doshi, R. Liston, W. tian Tan, X. Zhu, J. G. Andrews, and R. W. Heath, "DeepWiPHY: Deep Learning-based Receiver Design and Dataset for IEEE 802.11ax Systems," 2020.
- [27] Z. Zhou, L. Liu, and H.-H. Chang, "Learning for Detection: MIMO-OFDM Symbol Detection through Downlink Pilots," *preprint arXiv:1907.01516*, 2019.
- [28] 3GPP, "Evolved Universal Terrestrial Radio Access (E-UTRA); Base Station (BS) conformance testing," 3rd Generation Partnership Project (3GPP), Technical Specification (TS) 36.141, 2021. [Online]. Available: <https://portal.3gpp.org/desktopmodules/Specifications/SpecificationDetails.aspx?specificationId=2421>
- [29] R. W. Heath Jr and A. Lozano, *Foundations of MIMO communication*. Cambridge University Press, 2018.
- [30] P. Viswanath and D. N. C. Tse, "Sum capacity of the vector Gaussian broadcast channel and uplink-downlink duality," *IEEE Trans. Inform. Theory*, vol. 49, no. 8, pp. 1912–1921, 2003.
- [31] K. He, X. Zhang, S. Ren, and J. Sun, "Identity mappings in deep residual networks," in *Eur. Conf. Comput. vision*. Springer, 2016, pp. 630–645.
- [32] A. G. Howard, M. Zhu, B. Chen, D. Kalenichenko, W. Wang, T. Weyand, M. Andreetto, and H. Adam, "MobileNets: Efficient Convolutional Neural Networks for Mobile Vision Applications," *preprint arXiv:1704.04861*, 2017.
- [33] S. Jaeckel, L. Raschkowski, K. Börner, and L. Thiele, "QuaDRiGa: A 3-D Multi-Cell Channel Model With Time Evolution for Enabling Virtual Field Trials," *IEEE Trans. Antennas Propag.*, vol. 62, no. 6, pp. 3242–3256, 2014.
- [34] 3GPP, "Study on channel model for frequencies from 0.5 to 100 GHz," 3rd Generation Partnership Project (3GPP), Technical Report (TR) 38.901, 03 2017, version 14.2.2. [Online]. Available: <https://portal.3gpp.org/desktopmodules/Specifications/SpecificationDetails.aspx?specificationId=3173>
- [35] "IEEE Standard for Information technology - Local and metropolitan area networks - Specific requirements - Part 11: Wireless LAN Medium Access Control (MAC) and Physical Layer (PHY) Specifications," *IEEE Std 802.11n-2009*.
- [36] D. P. Kingma and J. Ba, "Adam: A Method for Stochastic Optimization," in *Proc. Int. Conf. Learn. Represent.*, 2015.